ACS NANO
Cite This: ACS Nano 2019, 13, 13709−13715
www.acsnano.org

ARTICLE

Self-Assembled Asymmetric Microlenses for Four-Dimensional Visual Imaging

Ling-Ling Ma,[†,∥] Sai-Bo Wu,[†,‡,∥] Wei Hu,[*,†,‡] Chao Liu,[†] Peng Chen,[†,‡] Hao Qian,[§] Yandong Wang,[⊥] Lifeng Chi,[⊥] and Yan-qing Lu[*,†]

[†]National Laboratory of Solid State Microstructures, Key Laboratory of Intelligent Optical Sensing and Manipulation, College of Engineering and Applied Sciences, and Collaborative Innovation Center of Advanced Microstructures, Nanjing University, Nanjing 210093, China

[‡]Institute for Smart Liquid Crystals, JITRI, Changshu 215500, China

[§]State Key Laboratory of Materials Oriented Chemical Engineering, College of Materials Science and Engineering, Nanjing Tech University, Nanjing 210009, China

[⊥]Jiangsu Key Laboratory for Carbon-Based Functional Materials Institute of Functional Nano & Soft Materials (FUNSOM), Soochow University, Suzhou 215123, China

Supporting Information

ABSTRACT: **Visual imaging that can extract three-dimensional (3D) space or polarization information on the target is essential in broad sciences and technologies. The simultaneous acquisition of them usually demands expensive equipment and sophisticated operations. Therefore, it is of great significance to exploit convenient approaches for four-dimensional (3D and polarization) visual imaging. Here, we present an efficient solution based on self-assembled asymmetric liquid crystal microlenses, with freely manipulated phase profiles and symmetry-breaking properties. Accordingly, characteristics of multifocal functionality and polarization selectivity are exhibited, along with the underlying mechanisms. Moreover, with a specific sample featured by radially increased unit sizes and azimuthally varied domain orientations, the discriminability of four-dimensional information is extracted in a single snapshot, *via* referring to the coordinates of the clearest images. Demultiplexing of depth/polarization information is also demonstrated. This work will unlock a variety of revolutionary apparatuses and lighten extensive applications.**

KEYWORDS: *liquid crystals, self-assembly, visual imaging, polarization detection, microlens array*

Visual imaging plays a vital role in human life, from a visual sense, medical imaging, microscopic observation, to astrosurveillance.[1−4] Usually, an imaging system is composed of a set of precisely aligned optical elements, by which the two-dimensional (2D) information on the object at the focal plane is captured.[5,6] To acquire the three-dimensional (3D) space information on the target, several practical techniques have been developed, such as confocal laser scanning microscopy (CLSM),[7] optical coherence tomography (OCT),[8,9] atomic force microscopy (AFM), and structured illumination microscopy (SIM).[10−12] The above apparatuses are enabled by the combination of laser techniques, ultrasensitive optoelectronic devices, high-precision automatic control, and reconstruction algorithms, thus they are commonly expensive, bulky, and time-consuming. Polarization, as another physical dimension of light, carries privileged information and is crucial in the characterization of materials,[13] remote sensing,[14] biology navigation, and intraspecific interaction.[15] For its detection, passive/active polarimeters or channeled spectropolarimeters are required.[16−18] If we were able to find a convenient way to simultaneously acquire both the 3D space and polarization information (*i.e.*, four-dimensional (4D) visual imaging), a variety of revolutionary apparatuses and applications over broad sciences and technologies would be unlocked. Unfortunately, until now, it has remained elusive.

Conventional optical lenses rely on the specific phase accumulation of light along the propagation in isotropic media.[19] Their focusing properties can be designed through presetting the curvatures of spherical or free-form lens surfaces. Nevertheless, compound eyes and ocelli of living beings further

Received: September 7, 2019
Accepted: November 4, 2019
Published: November 20, 2019

DOI: 10.1021/acsnano.9b07104
ACS Nano 2019, 13, 13709−13715

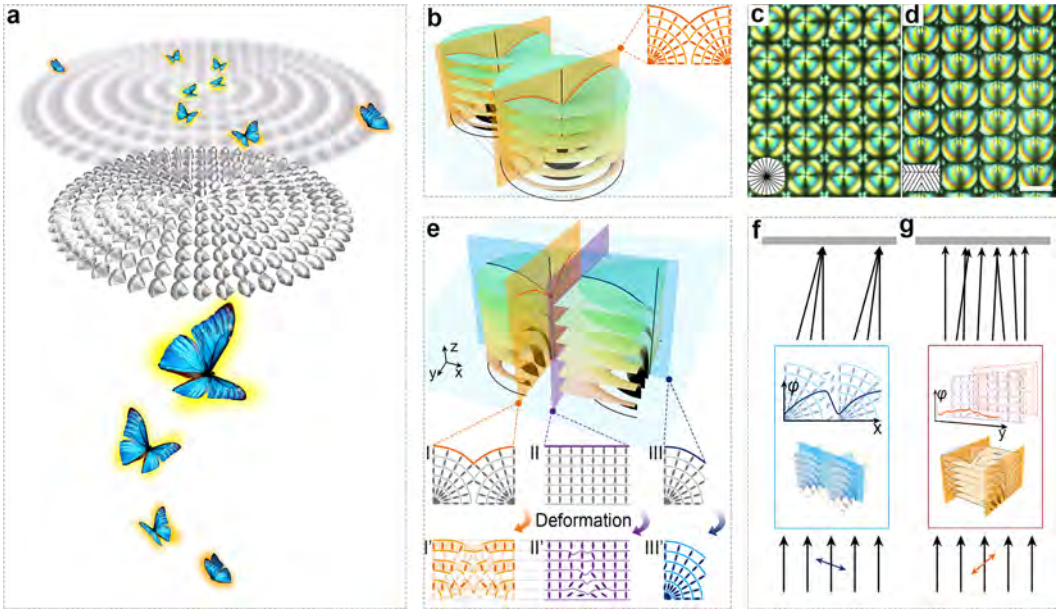

Figure 1. Configurations and optics of distorted LC superstructures. (a) Schematic of simultaneous acquisition of 3D space and polarization information *via* a distorted LC lens array. Four butterflies at the bottom represent objects in four different depths with their orientations indicating different polarization states. Four pairs of butterflies at the top represent images at the image plane. Their different locations are corresponding to different information carried (*i.e.*, depth and polarization). (b) 3D model of the curved smectic layers in toric focal conic domains (TFCDs). Inset shows sectional director field. (c,d) Textures of TFCDs and d-TFCDs under a polarized optical microscope. The photoalignment units are represented in the lower-left corners with the alignment direction denoted by lines. The scale bar indicates 10 μm. (e) 3D model of the curved smectic layers in d-TFCDs. The ideal and deformed sectional director distributions in $y-z$ and $x-z$ planes are shown as insets I, II, III and I′, II′, III′, respectively. The rods represent local LC directors, whereas the lines represent LC layers. (f,g) Phase profiles and influences on light propagation of d-TFCDs corresponding to x and y incident polarization, respectively. φ denotes the accumulated phase.

adopt gradient indices to flatten surfaces and optimize the imaging performance.[20] On the other hand, polarization detection is usually based on dichroic absorption, interface reflection, and birefringence. These strategies are also ubiquitously found in nature. For instance, mantis shrimps can perceive polarization attributed to a group of selectively absorptive microvilli in their torsional eyes.[15] Thanks to the tunable large birefringence and the controllable self-assembly behavior, liquid crystals (LCs) are very promising in imaging and polarization-dependent applications.[21−23] As the spatial refractive index distribution can be dynamically modulated, LC lenses with tunable focal lengths are achievable.[21,24] However, the polarization dependency of LC lenses is commonly unfavorable due to its influences on optical efficiency and imaging quality. Recently, researchers have started to present polarization-selective imaging elements with imperfect self-assembled configurations.[25,26] The above studies indicate that if the layouts of phase profiles and asymmetrical distortions of LC lenses were freely manipulated, one could acquire 4D information simultaneously on the basis of the locations of clearest images in a single snapshot (Figure 1a).

Here, we preprogram the curving of parallel LC layers to construct distortion-controllable microlenses and subsequently tailor the asymmetric phase profiles to visualize 4D information. Precisely manipulating the focal lengths of LC microlenses is enabled by delicately presetting the sizes of the photoalignment units. Their polarization selectivity is determined by the asymmetric distortions of the superstructures, whose orientation follows the underlying photoalignment unit direction. Correlative LC director distributions are schematically illustrated to reveal underlying mechanisms. After a specific photopatterned alignment with radially increased unit sizes and azimuthally varied unit directions is introduced, both the 3D space and polarization information on the target can be acquired according to the polar coordinates of the clearest images. The depth/polarization information demultiplexing is further demonstrated. This work will provide opportunities for displays, communications, biomedicine, military, and other emerging fields.

RESULTS AND DISCUSSION

Polarization Selectivity. Smectic LC (SLC) is featured by an ordered lamellar structure.[27−30] Under antagonistic anchoring conditions, parallel layers are periodically wrapped around defect lines to form a hexagonal toric focal conic domain (TFCD) array.[31−34] The ideal structure of TFCD exhibits perfect rotational invariance (Figure 1b). Its specific director field causes a gradient refractive index change and thus is capable of focusing light as a microlens array.[33,35,36] The lattice symmetry and size uniformity of TFCDs can be precisely manipulated *via* introducing multidomain photoalignment.[37] For instance, an ordered tetragonal TFCD array is presented (Figure 1c). The LC will always adjust its director distribution to minimize the free energy of the system. This enables the control of the superstructure distortion *via* changing the external stimuli including the anchoring condition. After altering the alignment condition, we observe distorted TFCDs (d-TFCDs) with gibbous-moon shapes (Figure 1d). It is an equilibrium state determined by multiple factors (elasticity, viscosity, and thickness of LC as well as external factors such as anchoring condition, thermal, and electrical field) at certain conditions. The ideal structure of

DOI: 10.1021/acsnano.9b07104
ACS Nano 2019, 13, 13709−13715

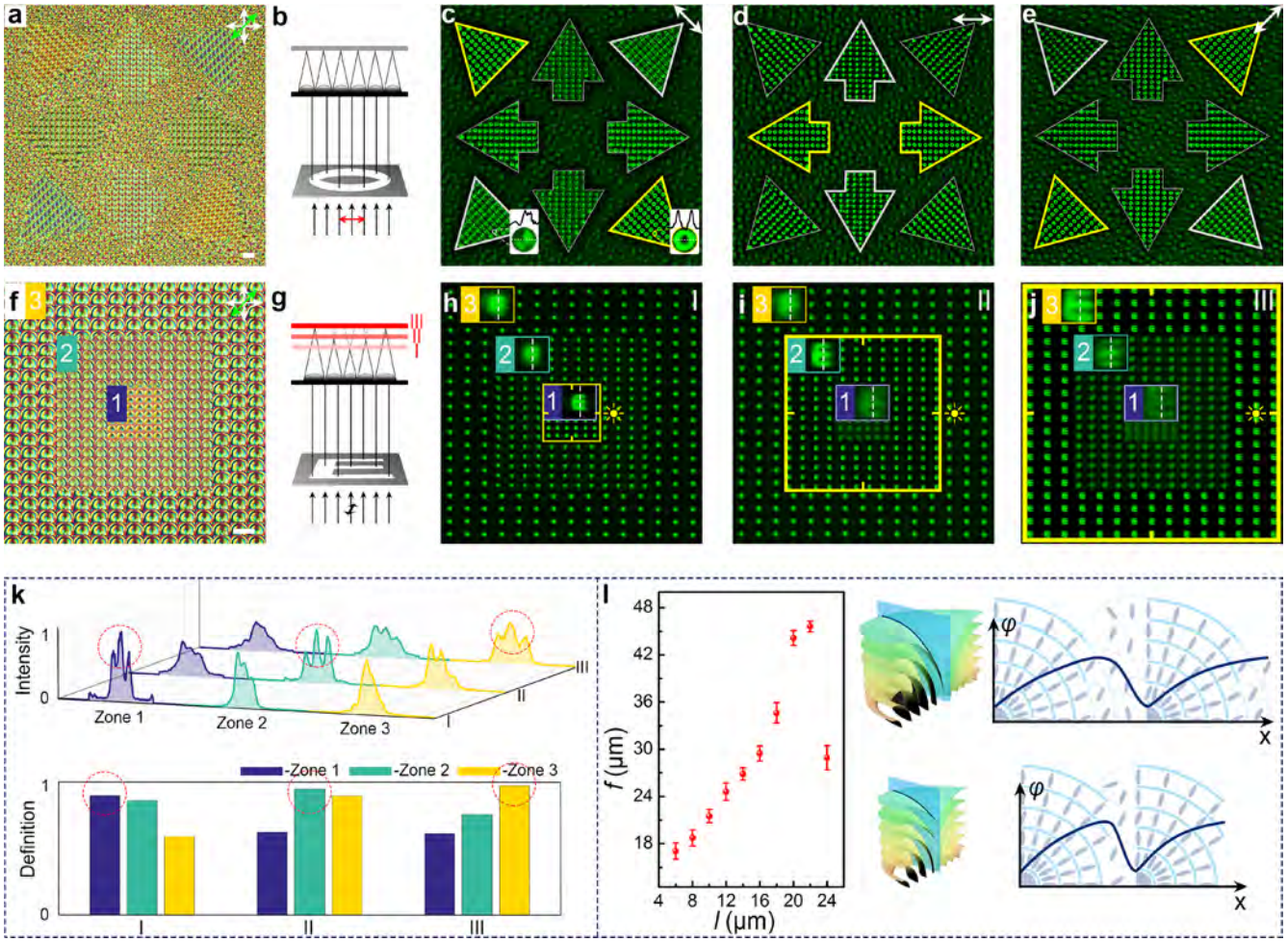

Figure 2. Polarization selectivity and multifocal functionality of d-TFCDs. (a) Polarized optical microscope texture of multidirectional d-TFCDs. The orientations of photoalignment units are consistent with arrows. (b) Schematic illustration of polarization-selective imaging. The polarization is alterable; d_o = 11.0 cm and d_i = 25.0 μm. (c−e) Images of a transmissive "O" mask for incident polarization of 135, 0, and 45°, separately. Insets in (c) show amplified "O" images with corresponding intensity profiles. (f) Polarized optical microscope texture of nested multisize d-TFCDs. (g) Schematic illustration of multifocal imaging. The image plane is alterable. (h−j) Images of a transmissive "E" mask at image planes of I, II, and III (d_o = 11.0 cm and d_i = 19.2, 25.0, and 29.7 μm, respectively). The polarization is 90°. (k) Quantified imaging quality analyses of images in (h−j). Red circles label the clearest "E" images. (l) Dependency of focal length on photoalignment unit size (mean ± SEM). 3D models and sectional director distributions in x−z planes of two different-sized d-TFCDs. The white and green arrows indicate the optical axes of the crossed polarizers and the tint plate, respectively. All scale bars are 20 μm.

adjacent segmented TFCDs is depicted in Figure 1e, and some cross sections of the director field are revealed in insets I, II, and III (neglecting the directors very close to the substrate, which will be strongly influenced by the anchoring condition of the alignment layer). Taking the deformations (resulted from the interactions between two adjacent domains) into account, we schematically illustrate corresponding sectional directors in insets I′, II′, and III′. Obviously, the directors in plane III′ are consistent with those in III, remaining a radially gradient index distribution. Considering the tiny depth of dimple-like singularities (∼100 nm) compared to the film thickness (several microns), its contribution to the phase accumulation is negligible. Therefore, a phase profile of a half convex lens is generated for x incident polarization (Figure 1f). Meanwhile, directors in planes I′ and II′ are distorted, and corresponding smectic layers fluctuate irregularly, making d-TFCDs lose the lensing effect for y incident polarization (Figure 1g). That means the symmetry-breaking superstructure results in a distinct polarization-selective imaging.

A specially designed multidirectional d-TFCD array is fabricated to verify the polarization selectivity. We rationally set the orientations of photoalignment units to make the symmetry axes of d-TFCDs parallel to their respective arrows (Figure 2a). Each unit is composed of four domains with alignment directions depicted by lines (±60°) (Figure 1d). Linearly polarized light transmits through an "O" mask (Figure S1a) and then is focused by the d-TFCD array (Figure 2b). We utilize a microscope to record "O" images for different incident polarization. Images from arrows parallel to the incident polarization are the clearest, whereas those from perpendicular arrows are the most blurred (Figure 2c−e and Figures S2 and S3). The imaging qualities of d-TFCDs in opposite arrows are equivalent. To give a more vivid comparison, typical "O" images are magnified, and corresponding intensity profiles are presented as insets (Figure 2c). The above phenomena indicate an intensive polarization selectivity of d-TFCDs, which is suitable for the visualization of polarization information.

DOI: 10.1021/acsnano.9b07104
ACS Nano 2019, 13, 13709−13715

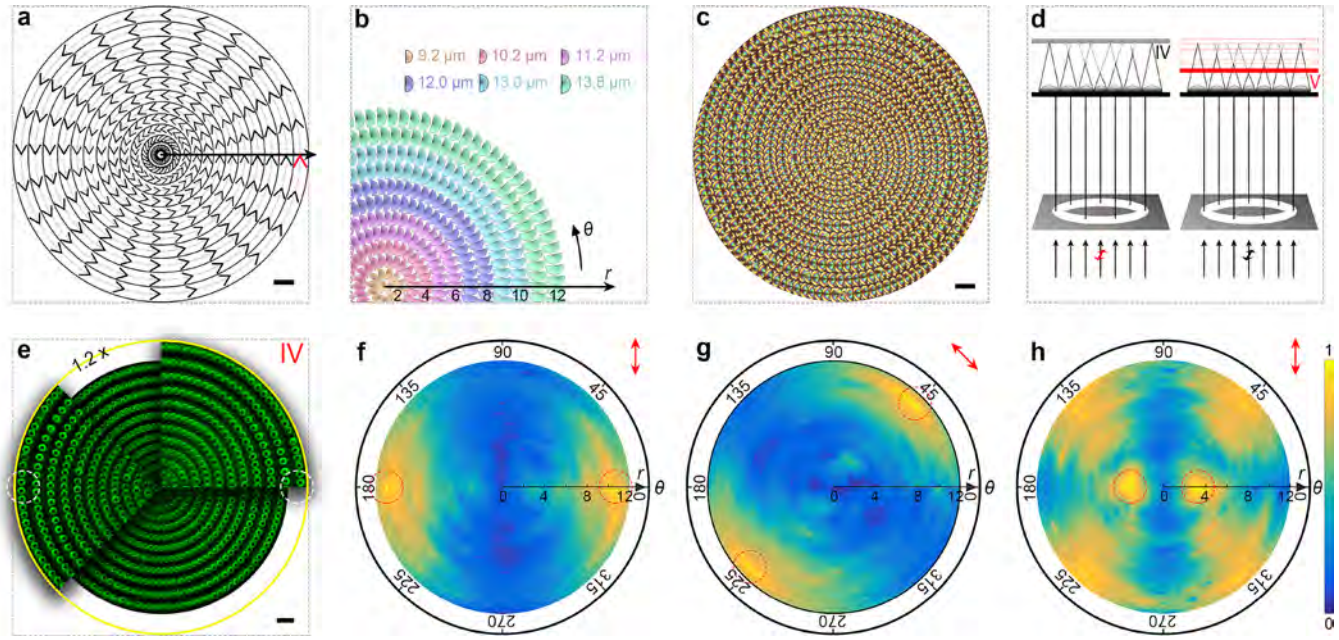

Figure 3. Extracting 4D information with multisize and orientation d-TFCDs. (a) Photoalignment pattern of the concentric d-TFCD array with the alignment direction denoted by lines. The two red lines direct at +60°/−60°. (b) Schematic of well-arranged d-TFCDs. (c) Polarized optical microscope texture of the sample. *r* denotes the ring number, and *θ* is the azimuthal angle. (d) Schematic illustration of polarization-selective and multifocal imaging with alterable components labeled in red. (e) Imaging pattern of a transmissive "O" mask for incident polarization of 90°. White circles indicate the clearest "O" images. (f−h) Image definition maps. d_o = 11.0 cm and d_i are 26.8, 26.8, and 20.2 μm. The polarization is 90, 135, and 90°, respectively. Red circles indicate the clearest "O" images. The color bar from dark blue to bright yellow represents the image definition from 0 to 1. All scale bars indicate 20 μm.

Multifocal Capability. The alignment confinement can also be applied to modulate the curvature of the phase profile of the d-TFCD, thus enabling the tunability of focal length (f). We produce nested multisized d-TFCDs (Figure 2f), whose diameters (D) in zones 1−3 are 8.3, 12.0, and 15.7 μm, respectively. Light with polarization parallel to the symmetry axes of d-TFCDs transmits through an "E" mask (Figure S1b) and then is focused by the sample (Figure 2g). As the image plane moves from I to III, the clearest "E" images appear from zone 1 to 3 sequentially (Figure 2h−j). Due to the centimeter-scale object distance d_o, which can be considered as infinite with respect to the micron-size image distance d_i, d_i is exactly the value of f. Blurred "E" images are either under-focused or over-focused. Sectional intensity profiles are extracted from typical "E" images in different zones (Figure 2k). Corresponding image definitions are calculated according to the edge detection algorithm to accurately quantify the imaging quality (supplementary text 1, Supporting Information). In addition, we systematically study the dependency of f (with polarization parallel to x direction of d-TFCDs) on the photoalignment unit size, here, the long side length (l). D obeys l within a certain range. Obviously, f increases along with l (Figure 2l and Figure S4). This originates from the flatter phase profile of the larger d-TFCD in a more relaxed anchoring confinement, as schematically illustrated by 3D models and sectional director distributions of two different-sized d-TFCDs. When l reaches 24 μm, f suddenly drops below 30 μm. In this case, the alignment unit is too roomy to generate a single d-TFCD, thus inducing several small fragmented domains. Meanwhile, due to the resolution limitation of our exposure system, the minimum l is 6 μm at present. On the basis of these facts, on-demand multifocal d-TFCDs could be precisely generated to acquire 3D space information, including the depth in the z direction.

Extracting 4D Information. To make full use of the polarization selectivity and multifocal capability of d-TFCDs, we propose a concentric d-TFCD array with radially increased sizes and azimuthally varied orientations. The sample is generated by spin-coating SLC onto the photoalignment layer with a concentrically aligned multiring pattern (Figure 3a). Within each ring, the alignment direction continuously varies with the azimuthal angle θ. Two adjacent alignment rings with the same widths but different alignment directions (±60°) are put together to determine both the size and the orientation of resultant d-TFCD. The structure of the formed d-TFCD array is schematically illustrated (Figure 3b). Two neighbored concentric d-TFCD rings are in an equal width, which is labeled in the same color as corresponding domains. The obtained SLC d-TFCD array is presented (Figure 3c). As expected, d-TFCDs concentrically coil around the center. Their sizes are consistent with the widths of coupled alignment rings and increase radially. Meanwhile, they orientate tangentially with respect to the dashed rings (Figure 3a).

For the imaging characterization, a linearly polarized light transmits through an "O" mask and the sample successively. We change the incident polarization to verify the polarization selectivity of the sample (Figure 3d, left; Figure S5a−d) and adjust the image plane to demonstrate its multifocal characteristic (Figure 3d, right; Figure S5e−h). A polar coordinate system is built based on r (the ring number as the polar radius) and θ (the azimuthal angle as the polar angle). Here, the clearest "O" images are observed at (11/12, 0°/180°) (Figure 3e). Images deteriorate gradually for positions away from (11/12, 0°/180°) as a result of the mismatch of the incident polarization and d_i. The corresponding image definition map is plotted to give a more vivid visualization (Figure 3f). After the incident polarization is rotated by 45°, coordinates of the

DOI: 10.1021/acsnano.9b07104
ACS Nano 2019, 13, 13709−13715

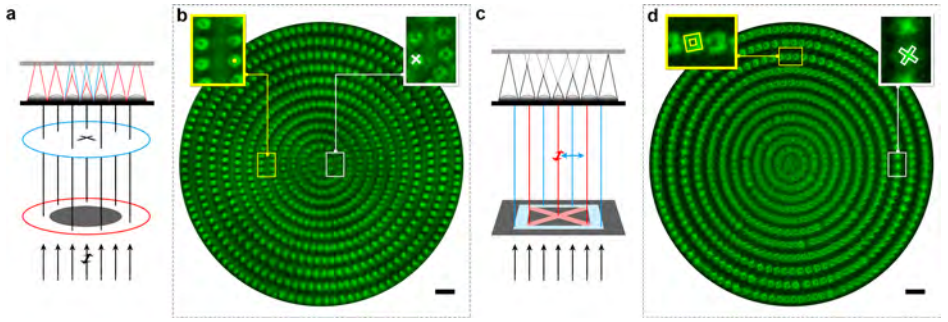

Figure 4. Depth/polarization information demultiplexing. (a) Schematic illustration of dual-object imaging. Incident polarization is 90°, and d_i is 25.0 μm. (b) Dual-object imaging pattern. The clearest images of the cross and the disc are 300% amplified. (c) Schematic illustration of dual-polarization imaging. Polarization of the cross and the square are 90 and 0°, respectively. d_o = 11 cm and d_i = 25.7 μm (d) Dual-polarization imaging pattern. The clearest images of the cross and the square is 300% amplified. Typical clearest images are outlined in yellow/white. All scale bars are 20 μm.

highest definition regions alter to (11/12, 45°/225°) accordingly (Figure 3g). On the other hand, when we move the image plane from IV to V, the clearest images appear at (3/4, 0°/180°) (Figure 3h). The other four regions with high image definition are observed at four corners of the map (Figure 3h). They are attributed to the partially effective lensing effect of nearly half the d-TFCD, exhibiting a shorter f and a position offset. Fortunately, such an issue can be satisfactorily addressed *via* optimizing the algorithm by taking the image position offset into consideration (Figure S6 and supplementary text 2, Supporting Information). The above results verify the capability of identifying the depth and polarization information on the target in addition to its 2D appearance *via* referring to the coordinates of the clearest images.

Demultiplexing of Depth/Polarization Information. To validate the capability of radially separating images with different depth information and azimuthally spreading out images with different polarization information, two specific targets are introduced. The first is a dual-object one composed of a cross and a disc, whose d_o values are 477 μm and 11 cm, respectively (Figure S1c,d). The 90° linearly polarized light transmits through the two objects consecutively and then is focused by the concentric d-TFCD array (Figure 4a) and captured at certain image plane (Figure 4b). Images are blurred for all under-focus and over-focus imaging conditions. Here, we find the clearest cross images at (1/2, 0°/180°), and the clearest disc images at (5/6, 0°/180°). The 0°/180° reveals that the incident polarization is 90°. The different r of the clearest images of the cross and the disc indicates the corresponding objects are located at different depths. The second is a dual-polarization target composed of a cross and a square with orthogonal polarization (Figure 4c and Figure S1e). The clearest cross and square images are at (9/10, 0°/180°) and (9/10, 90°/270°), respectively (Figure 4d). Therefore, the orthogonal incident polarization is azimuthally separated. Triple-polarization imaging is also demonstrated (Figure S7 and supplementary text 3 and supporting video). These supply a simple method for demultiplexing and visualizing both the depth and polarization information carried by the composite target.

By preprogramming 2D alignment confinements to guide the 3D asymmetric curving of LC layers, our research shows distorted SLC superstructures with free layouts of phase profiles and symmetry-breaking. These generated d-TFCDs are endowed with multifocal functionality and polarization selectivity, thus enabling the simultaneous determination of 4D information on the target. With the features of radially increased sizes and azimuthally varied orientations of d-TFCDs, 3D space information on an object is provided in a manner of spreading out clear images with different depth information radially. Meanwhile, the incident polarization can be distinguished according to the polar angles of coordinates of the clearest images. As vividly shown in the scheme (Figure 1a), for the four butterflies flying at different depths, whose reflections are polarization selective, their 4D information can be extracted and visualized *via* such distorted SLC microlenses. The above characteristics are attributed to the specific gradient refractive index distribution. The planar structure of d-TFCDs facilitates the device miniaturization and integration. The sophisticated distortions of SLC superstructures are carried out *via* self-assembly, guided by the preset 2D alignment, thus making the proposed method easy, efficient, and ready for volume production. As the distinction between orthogonal linear polarizations is most obvious, only linear-polarization mapping is presented here. Actually, as the orientation of each SmA lens can be arbitrarily and precisely controlled, full polarization detection can be reasonably expected. The proposed microlens array still suffers from restricted tunable range of size and imperfect phase profiles. Due to the responsivity of LC to various external stimuli, the phase profiles and symmetry-breaking properties of d-TFCDs can be further tuned. Such tunability effectively extends the tunable range and compensates the size discreteness between adjacent domains, thus enabling a continuous detection of depth information. The quality of phase profiles can also be improved *via* precisely tailoring the alignment conditions or introducing other confining techniques. Herein, SLC is utilized for a concept demonstration, and the 4D imaging is only related to the LC orientation. It is not restricted to d-TFCDs, and the same design can also be realized in other materials, such as nematic LCs, birefringent crystals, as well as artificial metasurfaces. That facilitates extending the range of lens size and corresponding focal length.

For practical application, we can introduce a polymerization strategy to make the asymmetric superstructures solid and self-standing, thus making the imaging characterization more feasible. In this case, images can be directly captured by a CCD placed behind the sample and precisely moved by a micromotor. The resolution of resultant images is still limited compared to that of commercial imaging systems.[38] Fortunately, it could be improved by introducing artificial

DOI: 10.1021/acsnano.9b07104
ACS Nano 2019, 13, 13709−13715

asymmetric microlenses with significantly improved phase profiles and further optimizing the computerized algorithm.[39,40] Such asymmetric microlenses provide a convenient method for visualizing 4D information on the target. By means of this technique, forward looking applications such as optical parallel detection, stereo-pico-projection, full-dimension autoaligning system, polarization-selective remote sensing, and information encryption could be expected.

CONCLUSION

In conclusion, we propose a strategy for 4D visual imaging with self-assembled asymmetric d-TFCDs. The focusing performance and polarization selectivity are rationally modulated *via* tailoring the alignment unit sizes and orientations, respectively. On the basis of the different-sized concentric d-TFCDs, the 3D space and polarization information can be visualized according to the polar coordinates (r and θ) of the clearest images. Moreover, the demultiplexing of depth/polarization information is also demonstrated. This work extends the understanding on the relationship between superstructures and functionalities of ordered soft matter. It may significantly upgrade existing optical apparatuses and inspire revolutionary applications across multiple fields.

MATERIALS AND METHODS

Fabrication of TFCD/d-TFCD Arrays. After multistep ultrasonic washing and UV-ozone cleaning, glass slides were spin-coated with SD1 (Dai-Nippon Ink and Chemicals, Japan). The alignment layers are annealed at 100 °C for 10 min. By means of a digital micromirror device based dynamic microlithography system,[41] they were photopatterned to perform the desired alignments. Subsequently, 8CB (HCCH, China) was cast onto the substrates and heated at 60 °C for 1 min, followed by a spin-coating process at 2400 rpm for 30 s. A special cooling from 38 °C (nematic phase) to 33 °C (smectic phase) at a rate of 0.2 °C/min was adopted to generate ideal TFCD/d-TFCD arrays.

Optical Characterization. Texture observations were performed using a polarized optical microscope (Nikon 50i, Japan) with or without a retardation plate (530 nm).

Imaging System. The lensing effect of d-TFCD arrays was characterized under a polarized optical microscope. We placed different objects (Figure S1) directly in front of the lamp, which is about 11 cm away from the microscope stage. A rotatable polarizer was applied to vary the state of linearly incident polarization. When the sample of distorted SLC superstructures was in focus, the image of the object could not be found. As the focus of microscope objective was moved upward, the texture of the sample gradually blurred and the image of the object became clear. To obtain higher image resolution, we used monochromatic incident light at 540 nm to avoid chromatic aberration during the imaging. A CCD was used to take imaging patterns.

The focal length of a gradient refractive index lens can be calculated by the equation of $f^{-1} = f_{GR}{}^{-1} + f_C{}^{-1}$, where f_{GR} represents the modulation of spatially varied refractive index and f_C represents the focal length determined by material-to-ambient refractive index difference and the curvature of lens surface. According to the previous study,[27] f_{GR} is on the order of micrometers for FCD microlenses, much smaller than the millimeter-scale f_C. Therefore, f approaches f_{GR} in this case. Here, to measure the focal length of d-TFCDs, objects were placed far away (11 cm) from the microscope stage. We first made the d-TFCD microlens arrays in focus and then moved the microscope objective to the image plane of d-TFCDs. As d_o can be regarded as infinite with respect to f, the moving distances of the microscope objective (*i.e.*, image distance d_i) are taken as the focal length of d-TFCD microlenses.

ASSOCIATED CONTENT

Supporting Information

The Supporting Information is available free of charge on the ACS Publications website at DOI: 10.1021/acsnano.9b07104.

Additional text on edge detection algorithm and triple-polarization imaging, as well as detailed polarized optical microscope images and imaging patterns of d-TFCDs (PDF)

Triple-polarization imaging with d-TFCDs (AVI)

AUTHOR INFORMATION

Corresponding Authors

*E-mail: huwei@nju.edu.cn.

*E-mail: yqlu@nju.edu.cn.

ORCID

Wei Hu: 0000-0003-1255-9453

Lifeng Chi: 0000-0003-3835-2776

Author Contributions

‖L.-L.M. and S.-B.W. contributed equally to this work.

Notes

The authors declare no competing financial interest.

ACKNOWLEDGMENTS

The authors gratefully acknowledge the support of the National Key Research and Development Program of China (2017YFA0303700), the National Natural Science Foundation of China (NSFC) (Nos. 61922038, 61575093, 61490714, and 61435008), and the Scientific Research Foundation of Graduate School of Nanjing University (2017ZDL06). W.H. appreciates the Distinguished Young Scholars Fund of Jiangsu Province (BK20180004) and the support of the Tang Scholar program.

REFERENCES

(1) Holler, M.; Guizar-Sicairos, M.; Tsai, E. H. R.; Dinapoli, R.; Müller, E.; Bunk, O.; Raabe, J.; Aeppli, G. High-Resolution Non-Destructive Three-Dimensional Imaging of Integrated Circuits. *Nature* **2017**, *543*, 402−406.

(2) Wang, S.; Wu, P. C.; Su, V.-C.; Lai, Y.-C.; Chen, M.-K.; Kuo, H. Y.; Chen, B. H.; Chen, Y. H.; Huang, T.-T.; Wang, J.-H.; et al. A Broadband Achromatic Metalens in the Visible. *Nat. Nanotechnol.* **2018**, *13*, 227−232.

(3) Stach, E. A. Real-Time Observations with Electron Microscopy. *Mater. Today* **2008**, *11*, 50−58.

(4) Li, X.; Kim, J.; Yoon, J.; Chen, X. Cancer-Associated, Stimuli-Driven, Turn on Theranostics for Multimodality Imaging and Therapy. *Adv. Mater.* **2017**, *29*, 1606857.

(5) Zhao, Q.; Yao, F.; Wang, Z.; Deng, S.; Tong, L.; Liu, K.; Zhang, J. Real-Time Observation of Carbon Nanotube Etching Process Using Polarized Optical Microscope. *Adv. Mater.* **2017**, *29*, 1701959.

(6) Khorasaninejad, M.; Chen, W. T.; Devlin, R. C.; Oh, J.; Zhu, A. Y.; Capasso, F. Metalenses at Visible Wavelengths: Diffraction-Limited Focusing and Subwavelength Resolution Imaging. *Science* **2016**, *352*, 1190−1194.

(7) Denk, W.; Strickler, J.; Webb, W. Two-Photon Laser Scanning Fluorescence Microscopy. *Science* **1990**, *248*, 73−76.

(8) Huang, D.; Swanson, E.; Lin, C.; Schuman, J.; Stinson, W.; Chang, W.; Hee, M.; Flotte, T.; Gregory, K.; Puliafito, C.; et al. Optical Coherence Tomography. *Science* **1991**, *254*, 1178−1181.

(9) Withers, P. J. X-Ray Nanotomography. *Mater. Today* **2007**, *10*, 26−34.

(10) Baykara, M. Z.; Schwendemann, T. C.; Altman, E. I.; Schwarz, U. D. Three-Dimensional Atomic Force Microscopy - Taking Surface Imaging to the Next Level. *Adv. Mater.* **2010**, *22*, 2838−2853.

(11) Graydon, O. 3D Displays: Momentum Multiplexing. *Nat. Photonics* **2016**, *10*, 570.
(12) Gustafsson, M. G. L. Surpassing the Lateral Resolution Limit by a Factor of Two Using Structured Illumination Microscopy. *J. Microsc.* **2000**, *198*, 82−87.
(13) Kim, D. S.; Čopar, S.; Tkalec, U.; Yoon, D. K. Mosaics of Topological Defects in Micropatterned Liquid Crystal Textures. *Sci. Adv.* **2018**, *4*, eaau8064.
(14) Powell, S. B.; Garnett, R.; Marshall, J.; Rizk, C.; Gruev, V. Bioinspired Polarization Vision Enables Underwater Geolocalization. *Sci. Adv.* **2018**, *4*, eaao6841.
(15) Daly, I. M.; How, M. J.; Partridge, J. C.; Temple, S. E.; Marshall, N. J.; Cronin, T. W.; Roberts, N. W. Dynamic Polarization Vision in Mantis Shrimps. *Nat. Commun.* **2016**, *7*, 12140.
(16) Arbabi, E.; Kamali, S. M.; Arbabi, A.; Faraon, A. Full-Stokes Imaging Polarimetry Using Dielectric Metasurfaces. *ACS Photonics* **2018**, *5*, 3132−3140.
(17) Osborne, I. S. Polarimetry Takes to a New Plane. *Science* **2016**, *351*, 930−930.
(18) Yuan, H.; Liu, X.; Afshinmanesh, F.; Li, W.; Xu, G.; Sun, J.; Lian, B.; Curto, A. G.; Ye, G.; Hikita, Y.; Shen, Z.; Zhang, S. C.; Chen, X.; Brongersma, M.; Hwang, H. Y.; Cui, Y. Polarization-Sensitive Broadband Photodetector Using A Black Phosphorus Vertical *p-n* Junction. *Nat. Nanotechnol.* **2015**, *10*, 707−713.
(19) Dong, L.; Agarwal, A. K.; Beebe, D. J.; Jiang, H. Adaptive Liquid Microlenses Activated by Stimuli-Responsive Hydrogels. *Nature* **2006**, *442*, 551−554.
(20) Land, M. F.; Nilsson, D. E. *Animal Eyes*; Oxford University Press: New York, 2002.
(21) Lin, H.-C.; Lin, Y.-H. An Electrically Tunable Focusing Liquid Crystal Lens with a Built-In Planar Polymeric Lens. *Appl. Phys. Lett.* **2011**, *98*, 083503.
(22) Rozic, B.; Fresnais, J.; Molinaro, C.; Calixte, J.; Umadevi, S.; Lau-Truong, S.; Felidj, N.; Kraus, T.; Charra, F.; Dupuis, V.; Hegmann, T.; Fiorini-Debuisschert, C.; Gallas, B.; Lacaze, E. Oriented Gold Nanorods and Gold Nanorod Chains within Smectic Liquid Crystal Topological Defects. *ACS Nano* **2017**, *11*, 6728−6738.
(23) Coursault, D.; Blach, J. F.; Grand, J.; Coati, A.; Vlad, A.; Zappone, B.; Babonneau, D.; Levi, G.; Felidj, N.; Donnio, B.; Gallani, J. L.; Alba, M.; Garreau, Y.; Borensztein, Y.; Goldmann, M.; Lacaze, E. Tailoring Anisotropic Interactions between Soft Nanospheres Using Dense Arrays of Smectic Liquid Crystal Edge Dislocations. *ACS Nano* **2015**, *9*, 11678−11689.
(24) Ren, H.; Lin, Y.-H.; Wu, S.-T. Adaptive Lens Using Liquid Crystal Concentration Redistribution. *Appl. Phys. Lett.* **2006**, *88*, 191116.
(25) Kim, Y. H.; Lee, J. O.; Jeong, H. S.; Kim, J. H.; Yoon, E. K.; Yoon, D. K.; Yoon, J. B.; Jung, H. T. Optically Selective Microlens Photomasks Using Self-Assembled Smectic Liquid Crystal Defect Arrays. *Adv. Mater.* **2010**, *22*, 2416−2420.
(26) Serra, F.; Gharbi, M. A.; Luo, Y.; Liu, I. B.; Bade, N. D.; Kamien, R. D.; Yang, S.; Stebe, K. J. Curvature-Driven, One-Step Assembly of Reconfigurable Smectic Liquid Crystal "Compound Eye" Lenses. *Adv. Opt. Mater.* **2015**, *3*, 1287−1292.
(27) Liarte, D. B.; Bierbaum, M.; Mosna, R. A.; Kamien, R. D.; Sethna, J. P. Weirdest Martensite: Smectic Liquid Crystal Microstructure and Weyl-Poincaré Invariance. *Phys. Rev. Lett.* **2016**, *116*, 147802.
(28) Yoon, D. K.; Kim, Y. H.; Kim, D. S.; Oh, S. D.; Smalyukh, I. I.; Clark, N. A.; Jung, H. T. Three-Dimensional Textures and Defects of Soft Material Layering Revealed by Thermal Sublimation. *Proc. Natl. Acad. Sci. U. S. A.* **2013**, *110*, 19263−19267.
(29) Gryn, I.; Lacaze, E.; Bartolino, R.; Zappone, B. Controlling the Self-Assembly of Periodic Defect Patterns in Smectic Liquid Crystal Films with Electric Fields. *Adv. Funct. Mater.* **2015**, *25*, 142−149.
(30) Gim, M. J.; Yoon, D. K. Orientation Control of Smectic Liquid Crystals *via* a Combination Method of Topographic Patterning and In-Plane Electric Field Application for a Linearly Polarized Illuminator. *ACS Appl. Mater. Interfaces* **2016**, *8*, 27942−27948.
(31) Kim, D. S.; Cha, Y. J.; Kim, M. H.; Lavrentovich, O. D.; Yoon, D. K. Controlling Gaussian and Mean Curvatures at Microscale by Sublimation and Condensation of Smectic Liquid Crystals. *Nat. Commun.* **2016**, *7*, 10236.
(32) Honglawan, A.; Beller, D. A.; Cavallaro, M.; Kamien, R. D.; Stebe, K. J.; Yang, S. Pillar-Assisted Epitaxial Assembly of Toric Focal Conic Domains of Smectic-A Liquid Crystals. *Adv. Mater.* **2011**, *23*, 5519−5523.
(33) Kim, Y. H.; Yoon, D. K.; Jeong, H. S.; Lavrentovich, O. D.; Jung, H.-T. Smectic Liquid Crystal Defects for Self-Assembling of Building Blocks and Their Lithographic Applications. *Adv. Funct. Mater.* **2011**, *21*, 610−627.
(34) Yoon, D. K.; Choi, M.; Kim, Y. H.; Kim, M. W.; Lavrentovich, O. D.; Jung, H.-T. Internal Structure Visualization and Lithographic Use of Periodic Toroidal Holes in Liquid Crystals. *Nat. Mater.* **2007**, *6*, 866−870.
(35) Honglawan, A.; Yang, S. Directing 3D Topological Defects in Smectic Liquid Crystals and Their Applications as an Emerging Class of Building Blocks. In *Nanoscience with Liquid Crystals: From Self-Organized Nanostructures to Applications*; Li, Q., Ed.; Springer International Publishing: Switzerland, 2014; Vol. *26*, pp 35−68.
(36) Kim, Y. H.; Jeong, H. S.; Kim, J. H.; Yoon, E. K.; Yoon, D. K.; Jung, H. T. Fabrication of Two-Dimensional Dimple and Conical Microlens Arrays From a Highly Periodic Toroidal-Shaped Liquid Crystal Defect Array. *J. Mater. Chem.* **2010**, *20*, 6557−6561.
(37) Ma, L. L.; Tang, M. J.; Hu, W.; Cui, Z. Q.; Ge, S. J.; Chen, P.; Chen, L. J.; Qian, H.; Chi, L. F.; Lu, Y. Q. Smectic Layer Origami *via* Preprogrammed Photoalignment. *Adv. Mater.* **2017**, *29*, 1606671.
(38) Wang, Z. L. New Developments in Transmission Electron Microscopy for Nanotechnology. *Adv. Mater.* **2003**, *15*, 1497−1514.
(39) He, Z. Q.; Lee, Y. H.; Chen, R.; Chanda, D.; Wu, S. T. Switchable Pancharatnam-Berry Microlens Array with Nano-Imprinted Liquid Crystal Alignment. *Opt. Lett.* **2018**, *43*, 5062−5065.
(40) Jiang, M.; Guo, Y.; Yu, H.; Zhou, Z.; Turiv, T.; Lavrentovich, O. D.; Wei, Q.-H. Low *f*-Number Diffraction-Limited Pancharatnam-Berry Microlenses Enabled by Plasmonic Photopatterning of Liquid Crystal Polymers. *Adv. Mater.* **2019**, *31*, 1808028.
(41) Wei, B. Y.; Hu, W.; Ming, Y.; Xu, F.; Rubin, S.; Wang, J. G.; Chigrinov, V. G.; Lu, Y. Q. Generating Switchable and Reconfigurable Optical Vortices *via* Photopatterning of Liquid Crystals. *Adv. Mater.* **2014**, *26*, 1590−1595.

DOI: 10.1021/acsnano.9b07104
ACS Nano 2019, 13, 13709−13715